Quaternary Chalcogenide-Based Misfit Nanotubes $LnS(Se)-TaS(Se)_2$ (Ln=La, Ce, Nd and Ho): Synthesis and Atomic Structural Studies

Luc Lajaunie[a,‡], *Gal Radovsky*[b,‡], *Reshef Tenne*[b,*] *and Raul Arenal*[a,c,*]

[a] Laboratorio de Microscopías Avanzadas, Instituto de Nanociencia de Aragón, Universidad de Zaragoza, 50018 Zaragoza, Spain.

[b] Department of Materials and Interfaces, Weizmann Institute of Science, 76100 Rehovot, Israel

[c] ARAID Foundation, 50018 Zaragoza, Spain.

ABSTRACT

We have synthesized quaternary chalcogenide-based misfit nanotubes LnS(Se)-TaS(Se)$_2$ (Ln=La, Ce, Nd and Ho). None of the compounds described here were reported in the literature as a bulk compound. The characterization of these nanotubes, at the atomic level, has been developed via different transmission electron microscopy techniques, including high-resolution scanning transmission electron microscopy, electron diffraction and electron energy loss spectroscopy. In particular, quantification at sub-nanometer scale was achieved by acquiring high-quality electron energy-loss spectra at high energy (~ between 1000 and 2500 eV). Remarkably, the sulfur was found to reside primarily in the distorted rocksalt LnS lattice, while the Se is associated with the hexagonal $TaSe_2$ site. Consequently, these quaternary misfit layered compounds (MLC) in the form of nanostructures possess a double superstructure of La/Ta and S/Se with the same periodicity. In addition, the interlayer spacing between the layers and the interatomic distances within the layer vary systematically in the nanotubes, showing clear reduction when going from the lightest (La atom) to the heaviest (Ho) atom. Amorphous layers, of different nature, were observed at the surface of the nanotubes. For La-based NTs, the thin external amorphous layer (inferior to 10 nm) can be ascribed to a Se-deficiency. Contrarily, for Ho-based NTs, the thick amorphous layer (between 10 and 20 nm) is clearly ascribed to oxidation. All these findings helped to understand the atomic structure of these new compounds and nanotubes thereof.

KEYWORDS: Misfit-layered compounds; Inorganic nanotubes; Atomic structure; Growth mechanism; HR-(S)TEM; EELS.

1. INTRODUCTION

Chalcogenide-based misfit layered compounds (MLC) of the general formula $(MX)_{1+y}(TX_2)_m$ (for simplicity designated as MX-TX_2), where (M=Sn, Pb, Sb, Bi, and rare earths; T=Nb, Ta, Ti, V, Cr; X=S, Se; $0.08 \leq y \leq 0.28$; m=1-3), have been investigated quite extensively.[1–5] The alternating TX_2 and MX layers, which are stacked periodically, have different crystallographic structure. While the MX unit has a distorted rocksalt structure, the TX_2 layer possess a hexagonal symmetry, in which the metal atoms are surrounded by six chalcogen atoms in octahedral or in trigonal prismatic coordination. In analogy to intercalation compounds, the rocksalt MX layer in MLC generally tends to adapt to the hexagonal layer. Its lattice parameters accommodates to the lattice parameter $\sim \sqrt{3}\cdot a$ of the TX_2 layer. Therefore, the (a-b) in-plane lattice parameters of the TX_2 subunit are conveniently indexed with ortho-pseudohexagonal unit cell with $a,\ b = a,\ \sqrt{3}\cdot a$. Since the ratio between a_{MX} and a_{TX2} is an irrational number, the MLC lattice has no unit cell and is represented for a convenience by an approximant.

Layered-based nanostructures are interesting due to intrinsic structural directionality owing to dissimilar interlayer and intralayer interactions.[6,7] Nanotubes of chalcogenide[8–13] and more recently oxide-based[14,15] misfit layered compounds were synthesized in recent years and their structures were elucidated in some detail. The MLC nanotubes are grown by chemical vapor transport (CVT) process along a very significant temperature gradient of about 600 ^{o}C. The main steps in the high-temperature growth of chalcogenide-based MLC nanotubes can be described as: (1) Assembly of the MLC clusters in the gas phase and growth on the substrate; (2) Relaxation of the misfit strain by folding of the nanostructures, and (3) Seaming of the layers into closed tubular layers. Presumably, while step 1 takes place close to the hot zone, step 3 occurs in the cold end of the ampoule. MLC lattices with high symmetry orthorhombic structure, such as GdS-CrS_2 and TbS-CrS_2 form more easily and produce nanotubes. On the other hand, nanoscrolls are abundant in low symmetry MLC crystals, such as LaS-CrS_2 with a triclinic structure.[10] LnS-TaS_2 and LnSe-$TaSe_2$ nanotubes,, where Ln stands for a lanthanide atom, were reported before.[13] In the present report tubular structures from quaternary LnS(Se)-TaS_2(Se) and LnS(Te)-TaS_2(Te) misfit layered compounds (MLC), where Ln stands for La, Ce, Nd and Ho, are reported. Remarkably, the sulfur is found to reside mostly in the distorted rocksalt LnS lattice, while the Se is associated primarily with the hexagonal $TaSe_2$ site. It should be mentioned that, in addition to the new nanotubular structures described in the present work, none of the compounds described here were reported in the literature as a bulk compound.

2. EXPERIMENTAL

2.1 Synthesis

For the synthesis of the LaS(Se)-TaS_2(Se), CeS(Se)-TaS_2(Se), NdS(Se)-TaS_2(Se) and the HoS(Se)-TaS_2(Se) tubular structures, Ta, Ln (La, Ce, Nd, Ho), S, Se, $TaCl_5$ powders were mixed at a molar ratio of ~ 1:1:1.5:1.5:0.1 and sealed in a quartz ampoule at ~ 5 x 10^{-5} torr. The powders used were purchased from the following companies and had the following purity: La, Ho (Strem Chemicals 99.9%), Nd (Strem Chemicals 99.8%), Ce (Alfa Aesar 99.9%), Ta (Alfa Aesar 99.9%), S (Sigma Aldrich 99.98%), Se (Fluka 99.9%), $TaCl_5$ (Alfa Aesar 99.8%). The ampoules were inserted into 1-zone vertical furnace and were held vertically. Two steps were performed: (1) The bottom edge of the ampoule with the precursors was kept at ~ 400 ^{o}C while the upper one at ~ 900 ^{o}C preventing the expansion of the precursors within the ampoule's volume and forcing pre-reaction. This step lasted for 1 hr. (2) The ampoule was moved within the furnace so its bottom edge with the precursors was kept at 900 ^{o}C and the upper edge at ~50 ^{o}C. This step lasted for 4 h. Afterwards, the ampoules were removed from the furnace rapidly and cooled at plain air. Most of the material remained at the hot bottom edge of the ampoule and the amount of the transported material was negligible.

The direct synthesis of the LaS(Te)-TaS2(Te) nanotubes from the pure elements was not possible. Therefore, an alternative procedure was adopted in this case, i.e. partial substitution of the sulfur by tellurium at elevated temperatures. For the synthesis of the LaS(Te)-TaS_2(Te) nanotubes, ~ 4 mgr of the powder product produced during the synthesis of the LaS-TaS_2 nanotubes (powder -1)[13] was mixed with 4 mg of Ta, 3 mg of La, 5.5 mg of Te (99.8% Sigma Aldrich) and 1 mg of $TaCl_5$ powders and sealed in ampoule at a vacuum of ~ 5 x 10^{-5} Torr. It was shown that powder -1 contains small amounts of binary phases and pure residual metal phases besides the ideal LaS-TaS_2 MLC.[13] However, if the assumed stoichiometry of powder 1 is assumed to be $TaLaS_3$, the molar ratio between the powder-1, Ta, La, Te and $TaCl_5$ is ~ 2.85:6.7:7.5:14:1. The ampoule was inserted into vertical 2-zone furnace and was held vertically. Two steps were performed. First: the bottom edge of the ampoule with the precursors was held at 400 ^{o}C while the upper at 900 ^{o}C, preventing the expansion of the precursors within the ampoule's volume and forcing pre-reaction. This step lasted for 1 h. At the second step the ampoule was moved within the furnace so its bottom edge with the material was at 830 ^{o}C and the upper edge was at 900 ^{o}C for 1 h. Note that the amount of the transported material was negligible. The yields of the nanotubes were ~50% for

LaS(Se)-TaS2(Se), ~20% for the CeS(Se)-TaS2(Se), 5% for NdS(Se)-TaS2(Se) and HoS(Se)-TaS2(Se), and ~1% for LaS(Te)-TaS2(Te).

2.2 Electron microscopy analysis

Zeiss Ultra model V55 scanning electron microscope (SEM) and LEO model Supra 55VP SEM equipped with EDS detector (Oxford model INCA) were utilized for the analysis of the products. Conventional transmission electron microscopy (TEM), including selected area electron diffraction (SAED) analyses, was performed using: a Philips CM120 TEM, operating at 120 kV and equipped with an EDS detector (EDAX-Phoenix Microanalyzer); a JEOL JEM2100 (operating at 200 kV) and a FEI Tecnai F30-UT HRTEM (operating at 300 kV). High-resolution scanning TEM (HR-STEM) imaging and spatially-resolved electron energy-loss spectroscopy (SR-EELS) were performed using a FEI Titan Low-Base microscope operated at 200 kV and equipped with a *Cs* probe corrector, a monochromator, an ultra-bright X-FEG electron source, an EDS detector and a Gatan Tridiem ESR 865 EELS spectrometer. HR-STEM imaging was performed by using high-angle annular dark-field (HAADF) and annular dark field (ADF) detectors. SR-EELS spectra were collected in STEM mode, using spectrum image and line scan modes.[16] The energy dispersion was 0.73 eV/pixel and the acquisition time was about 0.5 second/pixel. For most of the EELS experiments, the convergence and collection angles were 18 and 25 mrad, respectively. The EELS datasets were then de-noised with the open-source program Hyperspy by using principal component analysis routines.[17,18] This set-up allow us to acquire high quality spectra data at high energy (~ between 1000 and 2500 eV) with an acquisition total time inferior to 3 min while still being able to perform a proper quantification at sub-nanometer scale. The most representative spectra were submitted to the open-access EELS Database as references.[19]

3. RESULTS AND DISCUSSION

In this section, the details of the analyses of lanthanum-tantalum-chalcogenide MLC nanotubes are discussed. The results for the nanotubes with mixed chalcogenide MLC compounds of other lanthanide atoms (Ce, Nd and Ho) were not studied systematically. Hence much of the analyses of these MLC, other than the last section of this work, are presented in the supporting information (SI). The results of the analysis of the mixed chalcogenide LaS(Te)-TaS_2(Te) nanotubes included only SEM and TEM and are presented also in the SI.

Figure 1 shows the SEM images of LaS(Se)-$TaS(Se)_2$ nanotubes, whereas Figure S1 in the SI shows the SEM analysis of LnS(Se)-TaS_2(Se) nanotubes with Ln= Ce, Nd and Ho. The typical outer diameters of the LnS(Se)-TaS_2(Se) nanotubes varies between 50-200 nm which is smaller than their pure sulfide and selenide counterparts. Concentric tubes as well as scroll-like tubes were present in all LnS(Se)-TaS_2(Se) produced materials. Partially unfolded sheets as well as scrolling steps on the formed tubes are also clearly visible. Despite the fact that the selenium atom is larger than the sulfur atom, the average diameter of the mixed sulfur-selenium tubes is smaller than this one of the purely sulfur-based tubes. This trend can be possibly attributed to the larger strain in the mixed sulfur-selenium tubes, which is discussed below. The production yield of the tubular phases was calculated based on a statistical analysis of SEM images. They were ~50% for LaS(Se)-TaS_2(Se), ~20% for the CeS(Se)-TaS_2(Se), 5% for NdS(Se)-TaS_2(Se) and HoS(Se)-TaS_2(Se), and ~1% for LaS(Te)-TaS_2(Te).

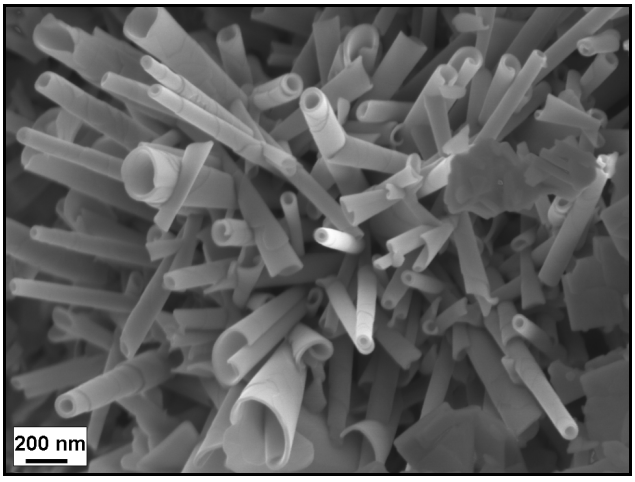

Figure 1. SEM image of the LaS(Se)-$TaS(Se)_2$ tubular structures and common by-products

Figure 2 shows the HRTEM and SAED analyses of a representative LaS(Se)-$TaS(Se)_2$ nanotube. Similar TEM analyses of tubes of the MLC compounds CeS(Se)-TaS_2(Se), NdS(Se)-TaS_2(Se) and HoS(Se)-$TaS(Se)_2$ are presented in the Supporting Information (Figure S2). The TEM analysis of the LaS(Te)-$TaS(Te)_2$ tubes is shown in Figure S3. All the nanotubes show a high degree of crystallinity. Their general structural aspects are analogous to the PbS-TaS_2[9] and PbS-NbS_2[10], LnS-TaS_2 and LaSe-$TaSe_2$[11] nanotubes. The SAED pattern of the tubule shown in Figure 2, exhibits twelve couples of 11.0 and 10.0 spots of TaX_2 suggesting two folding vectors. Since the multiplicity factors for these planes is six these equal-azimuthally distributed twelve couples of spots can be interpreted as two sextets marked by the red and orange small circles. These two

sextets of spots are azimuthally rotated by 30° (which is equivalent to 90° due to the symmetry 6 of these planes). This indicates the existence of two folding vectors for the pseudo-hexagonal $TaS(Se)_2$ layers of the nanotube. Also, there are two quartets of 110 and 220 spots of LnX (eight couples at all) indicating two folding vectors for the LnX layers. The structural details of the chalcogenide-based MLC nanotubes have been discussed extensively in the past[9–13] and will not be repeated here. More details can be nevertheless read in the SI. Semi-quantitative chemical (EDS) analyses of the tubules are shown in Figure S4 in the SI. The interplanar spacings of the diffraction spots were measured. The values of the interplanar spacing and interatomic distances of the $LaS(Se)$-$TaS(Se)_2$ deduced from the SAED patterns were found to vary between the pure sulfide and selenide counterparts[13] and are summarized in Table S1 in the SI. In general one sees that the interatomic distances are reduced when the atomic number of the lanthanide atom increases.

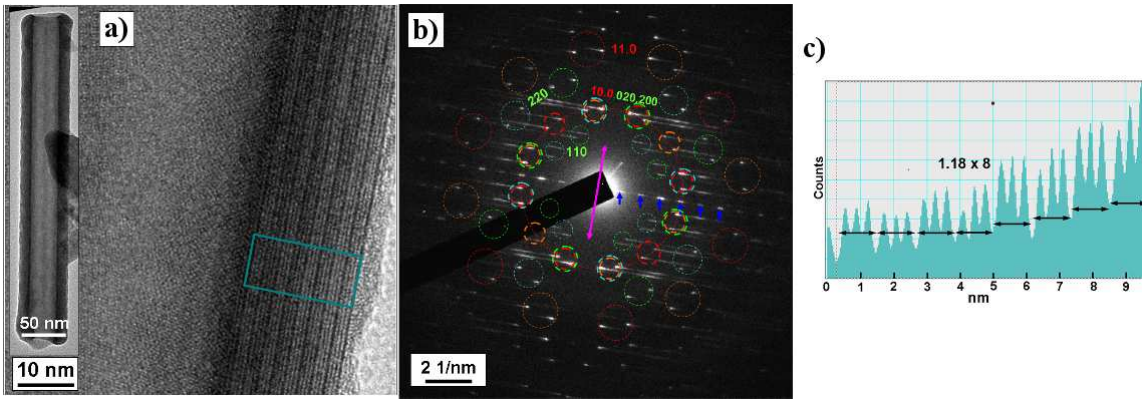

Figure 2. TEM analyses of $LaS(Se)$-$TaS(Se)_2$ nanotubes, with the two layers stacked periodically. Left: Low-magnification TEM image of one of those NTs. (a) High-magnification TEM micrograph of this NT. (b) SAED patterns acquired on this NT. Spots corresponding to the same interplanar spacings are marked by the same size circles (red and orange for TaS_2, green, azure and blue for LnS) and the respective Miller indices are indicated. The tubule axis is marked by purple double arrows. Basal reflections are marked by small blue arrows. Chiral angles of ~11.5° for the tubule were determined from the splitting of the spots.[9–11] (c) Line profile perpendicular to the tubule axe integrated along the rectangle marked in the Fig. 2 (a) TEM image.

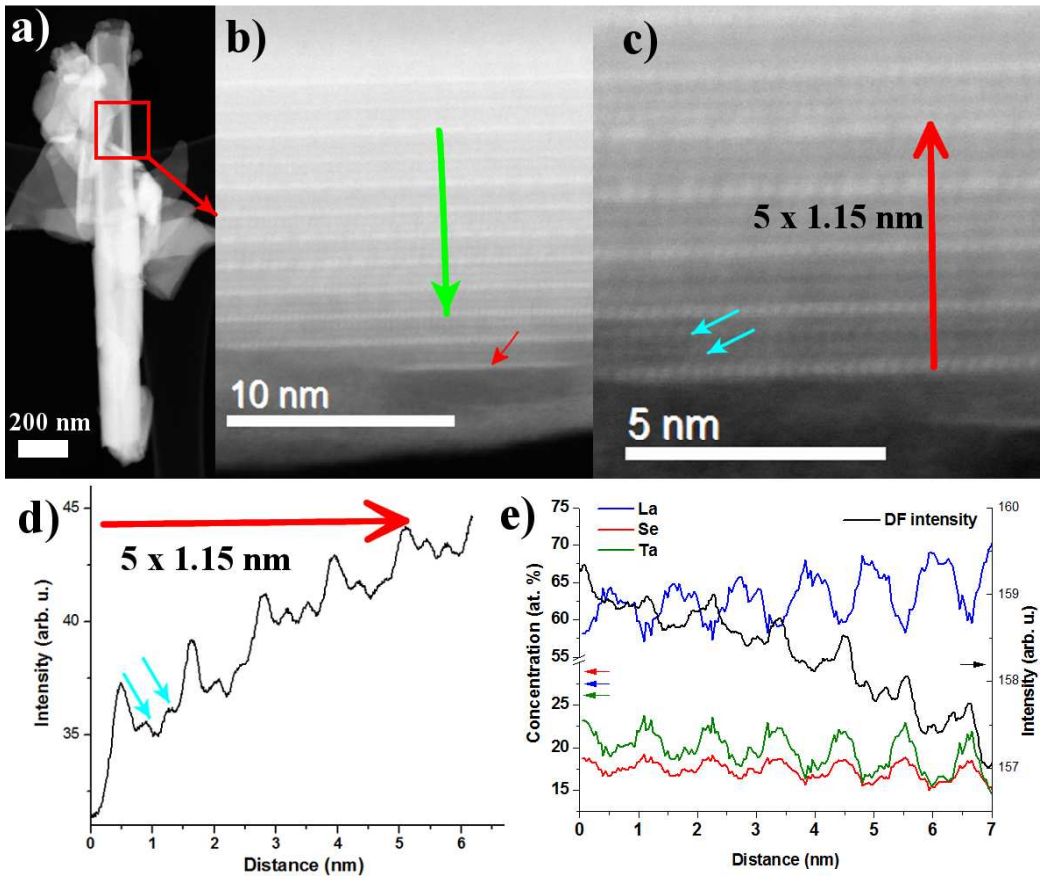

Figure 3 (a) Low-Magnification STEM ADF micrograph of a LaS(Se)-TaS(Se)$_2$ nanotube. The red square highlights the edge of the NT enhanced in **(b)** the HR-STEM ADF micrograph. The red arrow draws attention to the presence of low-order layer inside the external amorphous layer. **(c)** HR-STEM ADF image highlighting the 1.15 nm-periodicity of the bright layers. The red arrow indicates the area from which the **(d)** intensity profile was obtained. The blue arrows in Fig. 3(**c**) and (**d**) highlight the presence of a doublet of weaker intensities-layers between the bright layers. **(e)** Superposition of the elemental composition obtained from SR-EELS and the HR-STEM ADF intensity profile, both obtained from the area highlighted by a green arrow in Fig. 3(**b**). The blue, red and green lines correspond to the La, Se and Ta atomic concentrations, while the black line corresponds to the ADF intensity profile

Figure 3 and Figure S5 show the HR-STEM analyses of the LaS(Se)-TaS(Se)$_2$ nanotubes. The outer diameters are around one hundred nanometers and their lengths can reach more than one micron. Elemental quantification performed at the center of the NTs by EDS analyses (Figure S6) yields atomic ratios of 24, 23, 37 and 16 % for La, Ta, S and Se, respectively. This shows the 1:1 ratio between the La and Ta elements while the Se concentration seems to be deficient with respect to the S (Se) concentration. All the nanotubes show a high degree of crystallinity. In particular, an alternation of bright layers with a periodicity of 1.15 nm is clearly highlighted near the surface of the nanotubes, (Figures 3(b) and 3(c)). However, the average value of the interlayer

spacing measured for twelve nanotubes was higher, 1.19 ± 0.2 nm, and is in good agreement with the value obtained by electron diffraction (see Table S1 in the SI). Between the bright layers, a doublet of weaker intensities-layers can be distinguished (blue arrows in Figure 3(c)). Correspondingly with the LaS-TaS_2 nanotubes recently reported,[13] the bright layers in the ADF micrographs should belong to the Ta sub-system, while the darker (doublet) layers in-between correspond to the La sub-system. In order to check this point and to get significant chemical local information, SR-EELS spectrum-lines were recorded close to the surface of the NT (green arrow in Figure 3(b)). In addition to the elemental quantification, EELS allows to access a wealth of chemical information related to the local chemical bonding and valence states.[16,18–23] However, in the case of lamellar systems stacked into tubular structure, fine structure analysis are valid for the most external layers only and most of the information can be highlighted only through comparison of intensity ratio from one element to another and/or elemental quantification (if the cross-section are available).[12,14,15] The elemental composition was obtained using the La-$M_{4,5}$, Se-$L_{2,3}$ and Ta-$M_{4,5}$ edges situated at 824, 1435 and 1733 eV, respectively (see a representative spectrum in Figure 4). It is noteworthy that, in this case, the elemental composition obtained by EELS tends to overestimate the La atomic concentration, compared to the one obtained by EDS. This discrepancy might be ascribed to the precision of the computation of the partial cross-sections which is questionable for M shells[24], to the spectrometer aberrations present at such high dispersion and/or to the strong fine structures of the La edges when compared to the other edges. An accurate quantification by EELS requires using standard materials[25] however the meaning of an accurate quantification of incommensurate materials at the nanoscale is questionable. An alternative approach to reveal the structure at the local scale lies in the correlation between chemical and structural variations in the nanotube. This approach has been successfully applied to other misfit nanotubes.[14,15] The result of the SR-EELS elemental quantification is shown in Figure 3(e). As expected, there is a clear spatial anti-correlation between the area richer in La and that richer in Ta. The period between two consecutive areas richer in Ta is equal to 1.15 nm and corresponds to the higher values of the ADF intensity profile, which are thus ascribed to the bright layers. On the other hand, the areas richer in La match the lower values of the ADF intensity profile and are thus ascribed to the doublet of weaker intensities-layers. Concerning the distribution of S and Se between the La and Ta sub-systems, as the high temperature growth process is entropy driven, it could be expected that sulfur and selenium atoms are homogeneously distributed throughout the two sub-systems. In spite of that, the SR-EELS elemental quantification clearly shows that Se-rich areas are correlated with the Ta-rich area, indicating that the Se atoms are preferentially bonded to the Ta atoms. It can then be expected that S atoms are

preferentially bonded to the La atoms. However, due to the large energy separation between the La-$M_{4,5}$ and the S-$L_{2,3}$ edge (separated by 2470 eV), this hypothesis cannot be verified in a quantitative way, for this system.

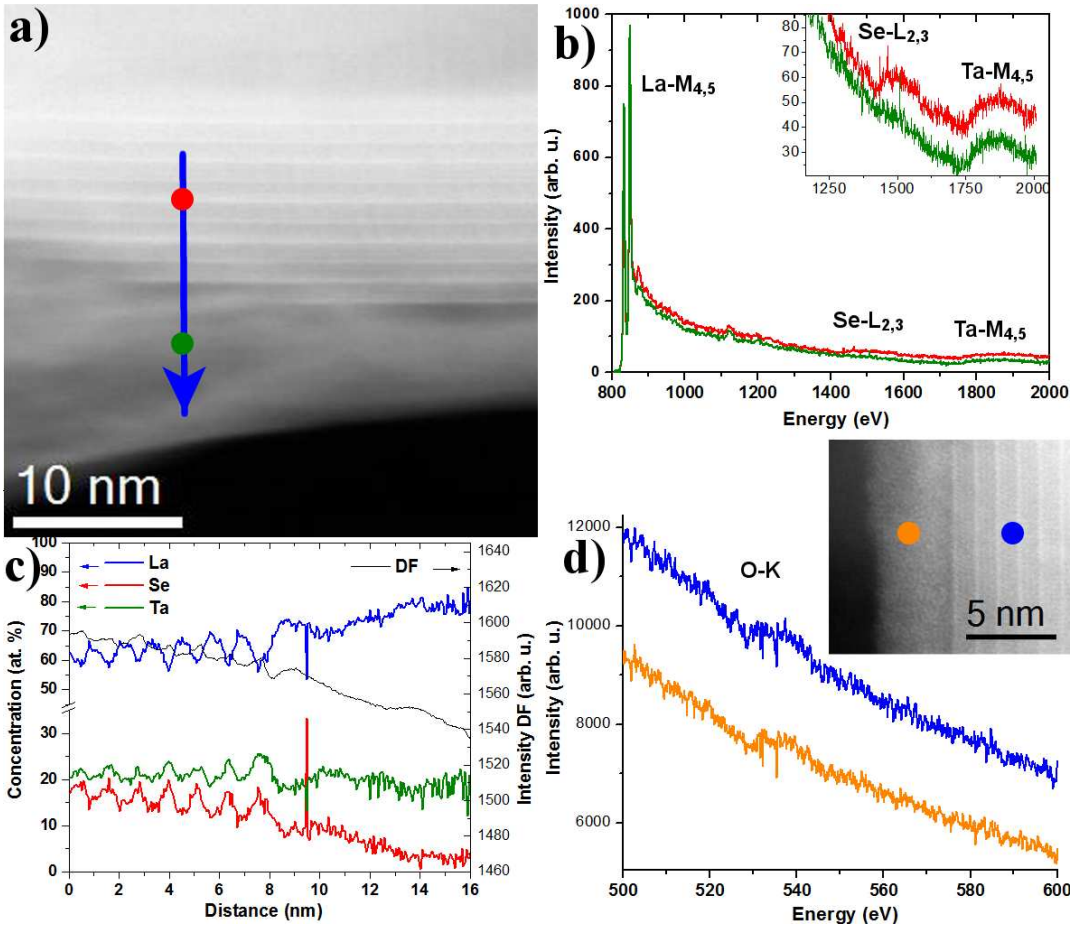

Figure 4 (a) HR-STEM ADF micrograph of the same LaS(Se)-TaS(Se)$_2$ nanotube shown in Figure S5(a). **(b)** EELS spectra showing the main edges used in this study for LaS(Se)-TaS(Se)$_2$ nanotubes. The red and green spectra had been taken on the areas highlighted by the red and green dots in Fig. 4(a), respectively. The inset shows a magnified view of the same spectra around the Ta-$M_{4,5}$ and Se-$L_{2,3}$ edges. **(c)** Elemental composition obtained from the SR-EELS line-scan highlighted by a blue arrow in Fig. 4(a). **(d)** EELS spectra showing the O-K edge. The blue and orange spectra had been taken on the areas highlighted by the blue and orange dots in the HR-STEM micrograph of the inset.

Finally, all the LaS(Se)-TaS(Se)$_2$ nanotubes show an external layer which is mainly amorphous (see also Figure S5). In several locations, fractions of crystalline layers embedded in the amorphous film on the nanotube surface could be resolved (see red arrow in Figure 3(b)). Depending on the nanotubes, the thickness of this external layer varied between 1 and 10 nm. The

EELS response of the crystalline area and the amorphous layer is clearly different (Figure 4). The La-$M_{4,5}$ signal is stronger in the crystalline part, while the Se-$L_{2,3}$ signal is weaker in the amorphous layer (the Se concentration reach 0 % at the surface of the NT). The Ta signal is similar in the crystalline and amorphous part of the nanotubes. Thus, the deficiency in Se in the amorphous layer explains the overall Se deficiency in the nanotube measured by EDS with regards to the S concentration. In addition, the electron-energy-loss near-edge fine structures (ELNES) of the O-K edge show no difference between the crystalline and amorphous regions (Figure S7(d)). The oxygen concentration is estimated to be around a few per cent in both areas. In this case, the external amorphous layer is not due to oxidation but to a deficiency in Se.

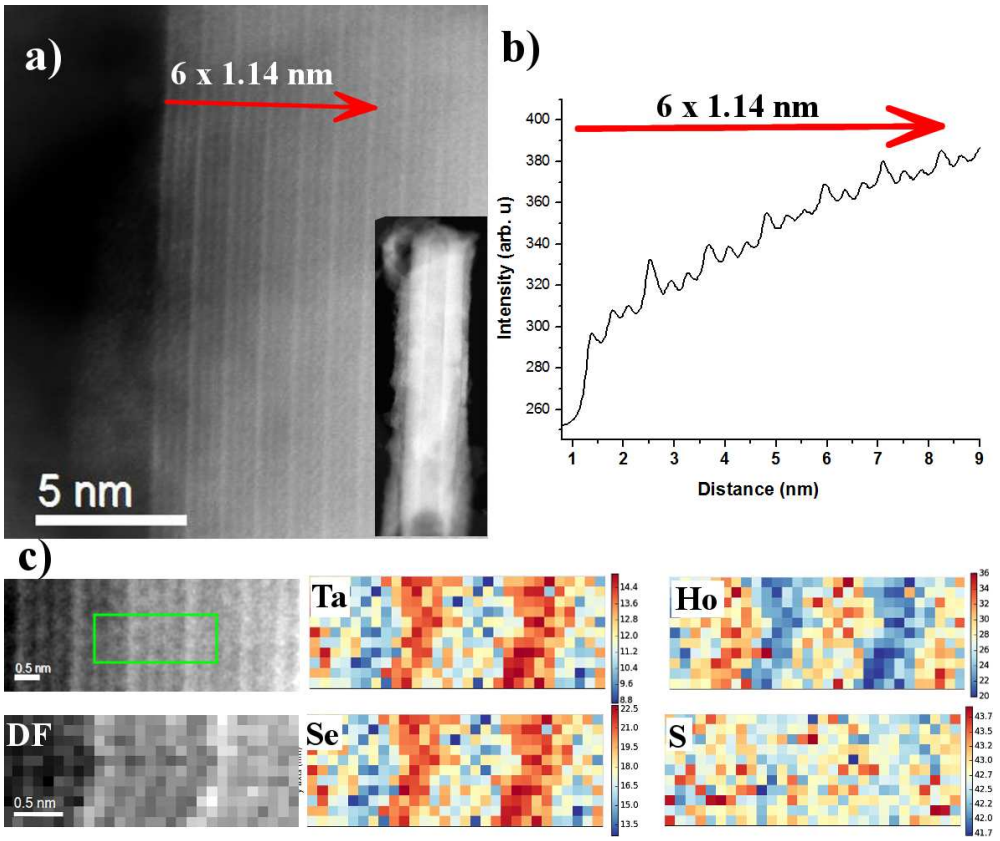

Figure 5 (a) HR- STEM ADF micrograph of a HoS(Se)-TaS(Se)$_2$ nanotube. The inset shows a low-magnification image of the NT. **(b)** Intensity profile obtained in the area highlighted by a red arrow in the Figure 5(a). **(c)** (From *top-left* to *bottom-right*) HR-STEM ADF micrograph, the green square highlights the area where a SR-EELS spectrum-image has been acquired. Map of the Ta atomic concentration obtained by EELS. Map of the Ho atomic concentration. Dark Field image. Map of the Se atomic concentration. Map of the S atomic concentration.

Recently, some of the syntheses reported in Ref. 13 and in the present work were repeated and the nanotubes were analyzed. It was clear that the nascent nanotubes were free of outer amorphous

film. If stored in a glovebox, the nanotubes did not develop the amorphous film with time. These experiments indicate that the nanotubes are gradually oxidized if stored for long time in the air, which was the practice used here. The formation of the Se-depleted amorphous layer on top of the nanotube surface is therefore believed to be an intermediate stage on the path to full oxidation. More work is needed to clarify the amorphization and subsequent oxidation mechanism of the nanotubes.

In order to check if the previous findings can be generalized to other quaternary misfit nanotubes, similar HR-STEM and SR-EELS analyses were conducted for HoS(Se)-TaS(Se)$_2$ nanotubes (Figures 5, S7 and S8). These nanotubes have a similar length to the LaS(Se)-TaS$_2$(Se) nanotubes (around 1 micron) and similar outer diameter (around one hundred nanometers). All these nanotubes are crystalline and show a similar alternation of bright layers and fainter doublet of dark layers (Figures 4(a) and 4(b)). The average periodicity of the bright layers measured on three nanotubes is 1.14 nm and is significantly smaller than that of LaS(Se)-TaS(Se)$_2$ NTs. The local chemical structure was investigated by SR-EELS spectrum-imaging by using the Ho-M$_{4,5}$, Se-L$_{2,3}$, Ta-M$_{4,5}$ and S-L$_{2,3}$ edges, which are at 1350, 1435, 1733 and 2470 eV, respectively (see a representative spectrum in Figure S8(a)). The results of the EELS elemental quantification are given in Figure 5(c). By comparing the ADF intensity map and the Ta and Ho chemical maps, it is clear that, in agreement with LaS(Se)-TaS(Se)$_2$ nanotubes, the bright layers can be ascribed to the Ta sub-system, while the layers consisting of a doublet of weaker intensities can be ascribed to the Ho sub-system. In addition, it is evident from Figure 4(c) that the Se and S atoms are preferentially bonded to the Ta and Ho atoms, respectively. The main difference between the two systems (LaS(Se)-TaS(Se)$_2$ and HoS(Se)-TaS(Se)$_2$) lies in the external amorphous layer, which is thicker in the case of HoS(Se)-TaS(Se)$_2$ nanotubes (between 8 and 20 nm). Some low-ordered layers can also be seen in this amorphous sheath (Figures S7(a) and S7(d)). The EELS response between the external amorphous layer and the crystalline part of the NT is, once again, completely different (Figure S8(a)). In analogy to LaS(Se)-TaS(Se)$_2$ nanotubes, a decrease of the Se-L$_{2,3}$ and S-L$_{2,3}$ signals in the amorphous layer is observed in the Ho-based nanotube. Indeed, the Se and S atomic concentrations at the surface of the nanotubes are close to 0 %. However, while the La-M$_{4,5}$ ELNES were similar for the amorphous and crystalline regions of the LaS(Se)-TaS(Se)$_2$ nanotubes, in the case of HoS(Se)-TaS$_2$(Se) nanotubes there is a great difference in the Ho-M$_{4,5}$ ELNES between the amorphous and the crystalline areas. In particular, a supplementary peak at 1370 eV is present in the crystalline region, whereas this peak is completely absent in the amorphous part (red arrow in the right inset of Figure S8(a)). A strong variation of the intensity ratio of the Ho M$_4$/M$_5$ can also be highlighted. These results suggest a strong variation of the local

chemical environment of the Ho atoms. Further EELS analyses show that it is induced by the oxygen atomic concentration, which is more than the double in the amorphous layer compared with the crystalline area (see Figures S8(c) and S8(d)). All these findings indicate that the HoS(Se)-TaS_2(Se) nanotubes are more prone to oxidation than their La counterparts. Experiments in progress (to be published elsewhere) with HoS-TaS_2 nanotubes clearly reveal the time evolution of this surface film, indicating that such nanotubes are prone to gradual oxidation-amorphization on their top and also inner surfaces. The present analysis shows that the oxygen concentration in the top amorphous film sheathing the nanotubes is not large. However, analysis of LaS-TaS_2 nanotubes which were left in the ambient for longer period of time (ca. two years), clearly revealed the surface oxidation and amorphization of the top nanotube surface. The kinetics of surface oxidation is likely to be influenced by the humidity and water adsorption on the nanotube surface. More research is needed to evaluate the mechanism of the gradual transformation of the crystalline MLC nanotubes into amorphous oxide phase. This observation stands in great contrast with the case of multiwall WS_2 nanotubes which exhibit no surface oxidation and degradation, whatsoever, at ambient conditions.

4. Conclusions

Nanotubes of the quaternary misfit layered compounds (MLC) belonging to the family LnS(Se)-$TaS(Se)_2$ with Ln=La, Ce, Nd and Ho, were synthesized in this work. These MLC compounds were not reported in the literature prior to this work, let alone in the nanotubular form. Careful SEM, and in particular high-resolution STEM imaging and EELS analyses indicate that the selenium atoms have great affinity to associate with the tantalum atoms while the sulfur atoms bind preferentially to the lanthanide atom. Consequently, these quaternary MLC nanostructures possess a double superstructure of La/Ta and S/Se with the same periodicity. Amorphous layers, of different nature, are observed at the surface of the nanotubes. For La-based NTs, the thin external amorphous layer (inferior than 10 nm) can be ascribed to a deficiency in Se without oxygen playing any role in his presence while for Ho-based NTs, the thick amorphous layer (between 10 and 20 nm) is clearly ascribed to oxidation. The interlayer spacing between the layers and the interatomic distances within the layer vary systematically in the nanotubes, showing clear reduction when going from the lightest (La atom) to the heaviest (Ho) atom. More research is needed to clarify the influence of the S-Se partition in the lattice of the MLC tubes on their electronic and optical properties.

ASSOCIATED CONTENT

Supporting Information. SEM image of the tubular structures. TEM images of the nanotubes. Measured interplanar spacings in tubular structures. TEM images of a LaS(Te)-$TaS(Te)_2$ nanotube. EDS spectra recorded from the nanotubes. HR-STEM micrographs of the LaS(Se)-$TaS(Se)_2$ nanotubes. EDS spectrum recorded from a LaS(Se)-$TaS(Se)_2$ nanotubes. HR-STEM micrographs of the HoS(Se)-$TaS(Se)_2$ nanotubes. HR-STEM and SR-EELS studies of one HoS(Se)-$TaS(Se)_2$ nanotube. "This material is available free of charge via the Internet at http://pubs.acs.org."

AUTHOR INFORMATION

Corresponding Authors

*Email: arenal@unizar.es ; reshef.tenne@weizmann.ac.il

Author Contributions

The manuscript was written through contributions of all authors. All authors have given approval to the final version of the manuscript. ‡These authors contributed equally.

Acknowledgements

The STEM (HR-ADF imaging, EDS and EELS) studies were conducted at the Laboratorio de Microscopias Avanzadas, Instituto de Nanociencia de Aragon, Universidad de Zaragoza, Spain. Some of the research leading to these results has received funding from the European Union H2020 program under the grant 696656 Graphene Flagship. R.A. gratefully acknowledges the support from the Spanish Ministry of Economy and Competitiveness (MINECO) through project grant MAT2016-79776-P, from the Government of Aragon and the European Social Fund under the project "Construyendo Europa desde Aragon" 2014-2020 (grant number E/26). The electron microscopy was performed at the Irving and Cherna Moscowitz Center for Nano and Bio-Nano Imaging of the Weizmann Institute of Science grant No. 7208214. We acknowledge the support of the Perlman Family Foundation; the Kimmel Center for Nanoscale Science grant No. 43535000350000; the German-Israeli Foundation (GIF) grant No. 712053; the Irving and Azelle Waltcher Foundations in honor of Prof. M. Levy grant No. 720821,

References

(1) Wiegers, G.; Meerschaut, A. Structures of Misfit Layer Compounds (MS)NTS2 (M= Sn, Pb, Bi, Rare Earth Metals; T= Nb, Ta, Ti, V, Cr; 1.08< N< 1.23). *J. Alloys Compd.* **1992**, *178*, 351–368.

(2) Williams, T.; Hyde, B. Electron Microscopy of Cylindrite and Franckeite. *Phys. Chem. Miner.* **1988**, *15*, 521–544.

(3) Putri, Y. E.; Wan, C.; Wang, Y.; Norimatsu, W.; Kusunoki, M.; Koumoto, K. Effects of Alkaline Earth Doping on the Thermoelectric Properties of Misfit Layer Sulfides. *Scr. Mater.* **2012**, *66*, 895–898.

(4) Landa-Cánovas, A.; Gómez-Herrero, A.; Otero-Díaz, L. C. Electron Microscopy Study of Incommensurate Modulated Structures in Misfit Ternary Chalcogenides. *Micron* **2001**, *32*, 481–495.

(5) Grippa, A. Y.; Lidin, S.; D'yachenko, O. G.; Rupasov, D. P.; Antipov, E. V. Synthesis and Study of Sr-Substituted Misfit Layer Sulfides. *Mater. Res. Bull.* **2005**, *40*, 79–91.

(6) Chatterjee, A.; Biswas, K. Solution-Based Synthesis of Layered Intergrowth Compounds of the Homologous PbmBi2nTe3n+m Series as Nanosheets. *Angew. Chem. Int. Ed.* **2015**, *54*, 5623–5627

(7) Banik, A.; Biswas, K. Synthetic Nanosheets of Natural van Der Waals Heterostructures. *Angew. Chem. Int. Ed.* **2017**, *56*, 14561–14566.

(8) Hong, S. Y.; Popovitz-Biro, R.; Prior, Y.; Tenne, R. Synthesis of SnS2/SnS Fullerene-like Nanoparticles: A Superlattice with Polyhedral Shape. *J. Am. Chem. Soc.* **2003**, *125*, 10470–10474.

(9) Radovsky, G.; Popovitz-Biro, R.; Tenne, R. Nanotubes from the Misfit Layered Compounds MS-TaS2, Where M= Pb, Sn, Sb and Bi: Synthesis and Study of Their Structure. *Chem. Mater.* **2014**, *26*, 3757--3770.

(10) Radovsky, G.; Popovitz-Biro, R.; Stroppa, D. G.; Houben, L.; Tenne, R. Nanotubes from Chalcogenide Misfit Compounds: Sn–S and Nb–Pb–S. *Acc. Chem. Res.* **2014**, *47*, 406–416.

(11) Panchakarla, L. S.; Radovsky, G.; Houben, L.; Popovitz-Biro, R.; Dunin-Borkowski, R. E.; Tenne, R. Nanotubes from Misfit Layered Compounds: A New Family of Materials with Low Dimensionality. *J. Phys. Chem. Lett.* **2014**, *5*, 3724–3736.

(12) Panchakarla, L. S.; Lajaunie, L.; Tenne, R.; Arenal, R. Atomic Structural Studies on Thin Single-Crystalline Misfit-Layered Nanotubes of TbS-CrS2. *J. Phys. Chem. C* **2016**, *120*, 15600–15607.

(13) Radovsky, G.; Popovitz-Biro, R.; Lorenz, T.; Joswig, J.-O.; Seifert, G.; Houben, L.; Dunin-Borkowski, R. E.; Tenne, R. Tubular Structures from the LnS–TaS2 (Ln= La, Ce, Nd, Ho, Er) and LaSe–TaSe2 Misfit Layered Compounds. *J. Mater. Chem. C* **2016**, *4*, 89–98.

(14) Panchakarla, L. S.; Lajaunie, L.; Ramasubramaniam, A.; Arenal, R.; Tenne, R. Nanotubes from Oxide-Based Misfit Family: The Case of Calcium Cobalt Oxide. *ACS Nano* **2016**, *10*, 6248–6256.

(15) Panchakarla, L. S.; Lajaunie, L.; Ramasubramaniam, A.; Arenal, R.; Tenne, R. Strontium Cobalt Oxide Misfit Nanotubes. *Chem. Mater.* **2016**, *28*, 9150–9157.

(16) Jeanguillaume, C.; Colliex, C. Spectrum-Image: The next Step in EELS Digital Acquisition and Processing. *Ultramicroscopy* **1989**, *28*, 252–257.

(17) Peña, F. de la; Burdet, P.; Ostasevicius, T.; Sarahan, M.; Nord, M.; Taillon, V. T. F. J.; Eljarrat, A.; Mazzucco, S.; Donval, G.; Zagonel, L. F.; Walls, M.; Iyengar, I. *HyperSpy: Multidimensional Data Analysis Toolbox*; 2015.

(18) Arenal, R.; De la Pena, F.; Stephan, O.; Walls, M.; Tence, M.; Loiseau, A.; Colliex, C. Extending the Analysis of EELS Spectrum-Imaging Data, from Elemental to Bond Mapping in Complex Nanostructures. *Ultramicroscopy* **2008**, *109*, 32–38.

(19) Ewels, P.; Sikora, T.; Serin, V.; Ewels, C. P.; Lajaunie, L. A Complete Overhaul of the Electron Energy-Loss Spectroscopy and X-Ray Absorption Spectroscopy Database: Eelsdb. Eu. *Microsc. Microanal.* **2016**, *22*, 717–724.

(20) Gross, K.; Barragán, J. P.; Sangiao, S.; De Teresa, J.; Lajaunie, L.; Arenal, R.; Calderón, H. A.; Prieto, P. Electrical Conductivity of Oxidized-Graphenic Nanoplatelets Obtained from Bamboo: Effect of the Oxygen Content. *Nanotechnology* **2016**, *27*, 365708.

(21) Hanson, E. D.; Lajaunie, L.; Hao, S.; Myers, B. D.; Shi, F.; Murthy, A. A.; Wolverton, C.; Arenal, R.; Dravid, V. P. Systematic Study of Oxygen Vacancy Tunable Transport Properties of Few-Layer MoO3-x Enabled by Vapor-Based Synthesis. *Adv. Funct. Mater.* **2017**, *27* (17).

(22) Lajaunie, L.; Pardanaud, C.; Martin, C.; Puech, P.; Hu, C.; Biggs, M. J.; Arenal, R. Advanced Spectroscopic Analyses on a: CH Materials: Revisiting the EELS Characterization and Its Coupling with Multi-Wavelength Raman Spectroscopy. *Carbon* **2017**, *112*, 149–161.

(23) Arenal, R.; March, K.; Ewels, C.P.; Rocquefelte, X.; Kociak, M.; Loiseau, A.; Stéphan, O. Atomic Configuration of Nitrogen-Doped Single-Walled Carbon Nanotubes, *Nano Lett.* **2014**, 14, 5509–5516.

(24) Egerton, R. F. *Electron Energy-Loss Spectroscopy in the Electron Microscope*; Springer Science+Business Media: New York, 2011.

(25) Lajaunie, L.; Boucher, F.; Dessapt, R.; Moreau, P. Quantitative Use of Electron Energy-Loss Spectroscopy Mo-M2,3 Edges for the Study of Molybdenum Oxides. *Ultramicroscopy* **2015**, *149*, 1–8.

For Table of Contents Only

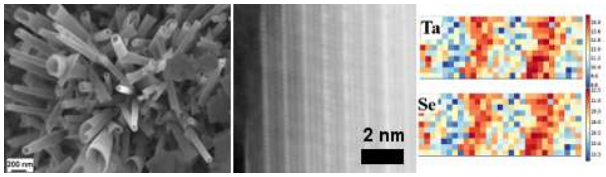

Synthesis and a detailed structural and compositional characterization of quaternary chalcogenide-based misfit nanotubes:

Left: SEM image of the LaS(Se)-TaS(Se)$_2$ tubular structures and common by-products. *Middle:* HR-STEM ADF micrograph of a HoS(Se)-TaS(Se)$_2$ nanotube. *Right:* Ta and Se atomic concentration maps obtained by EELS.

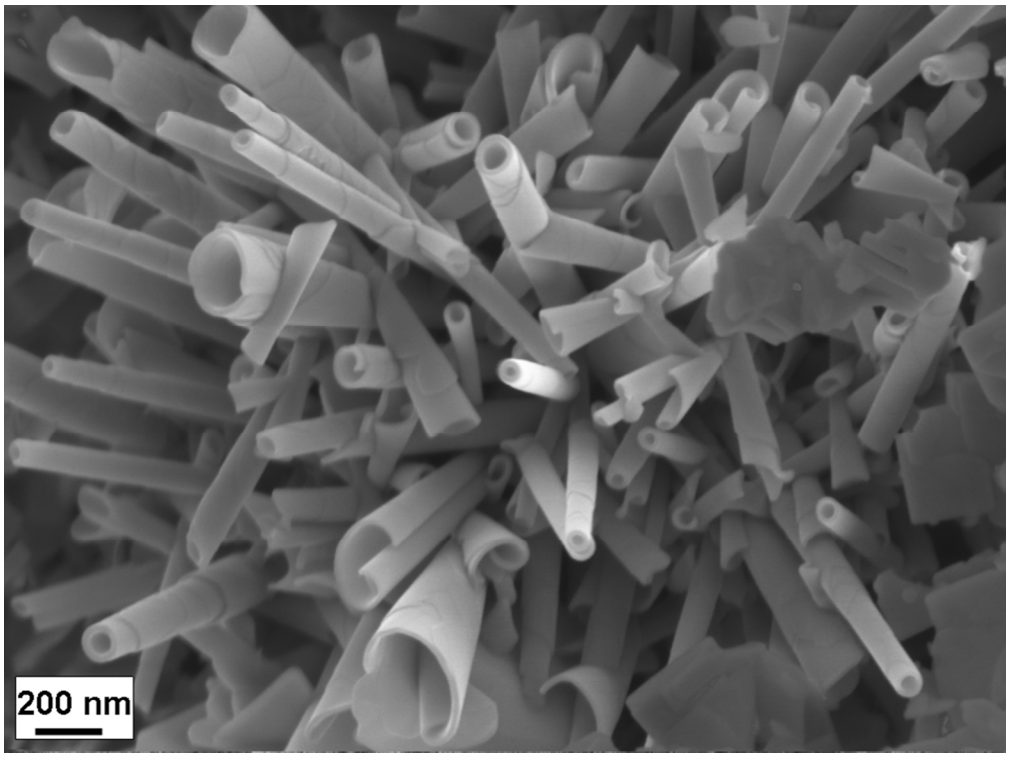

181x135mm (135 x 135 DPI)

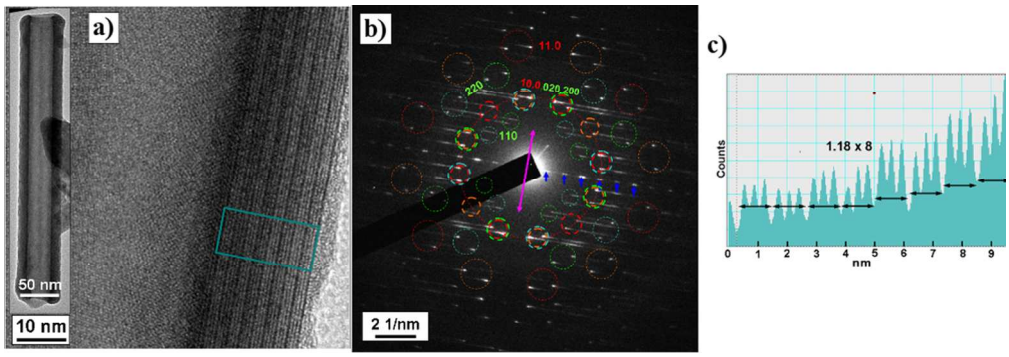

321x111mm (90 x 90 DPI)

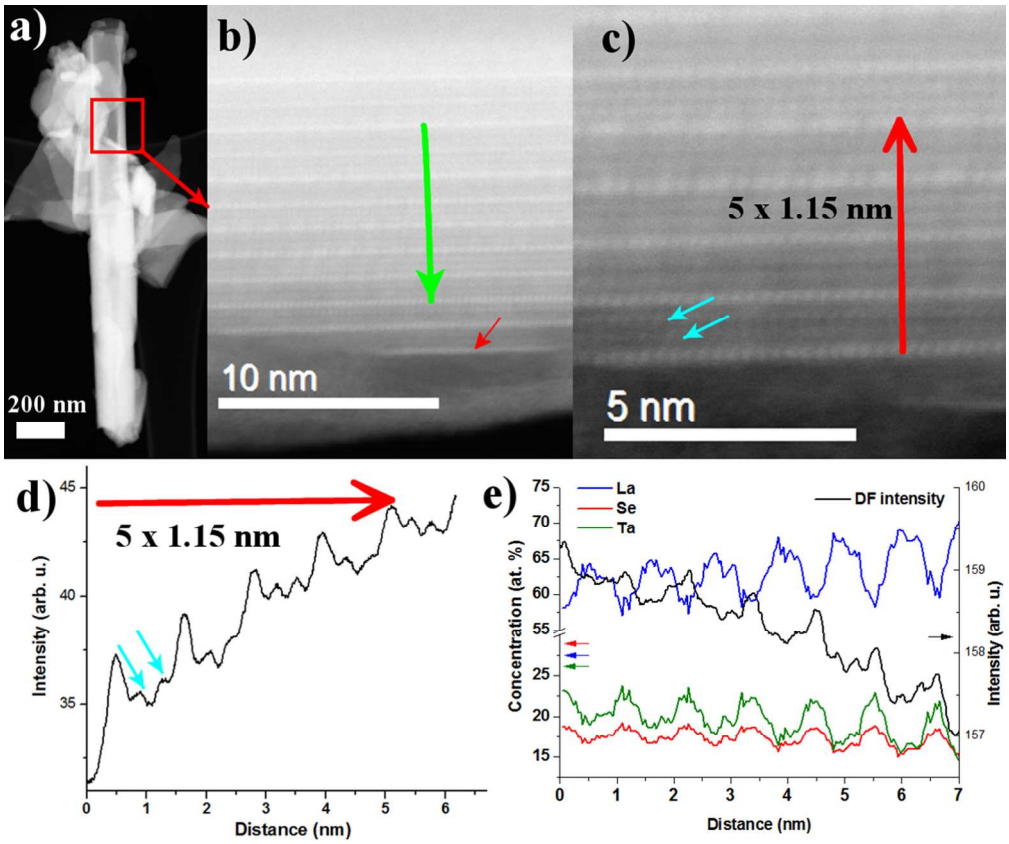

226x190mm (133 x 132 DPI)

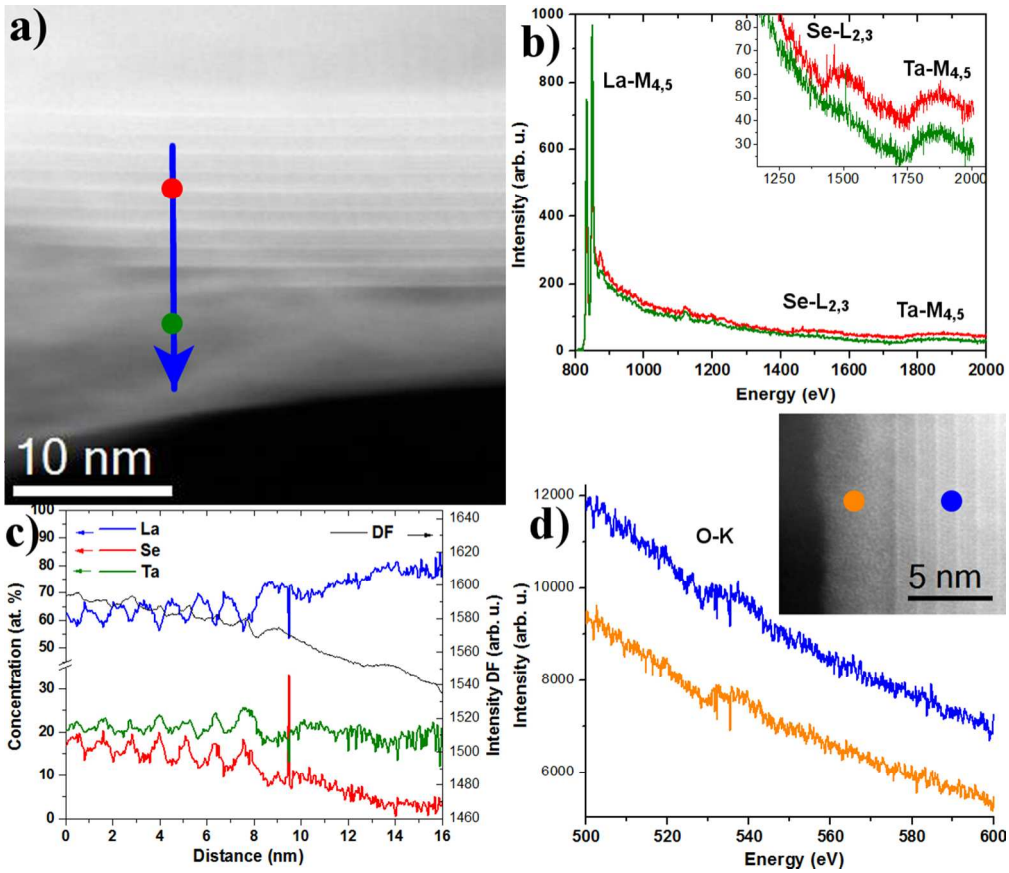

222x191mm (135 x 135 DPI)

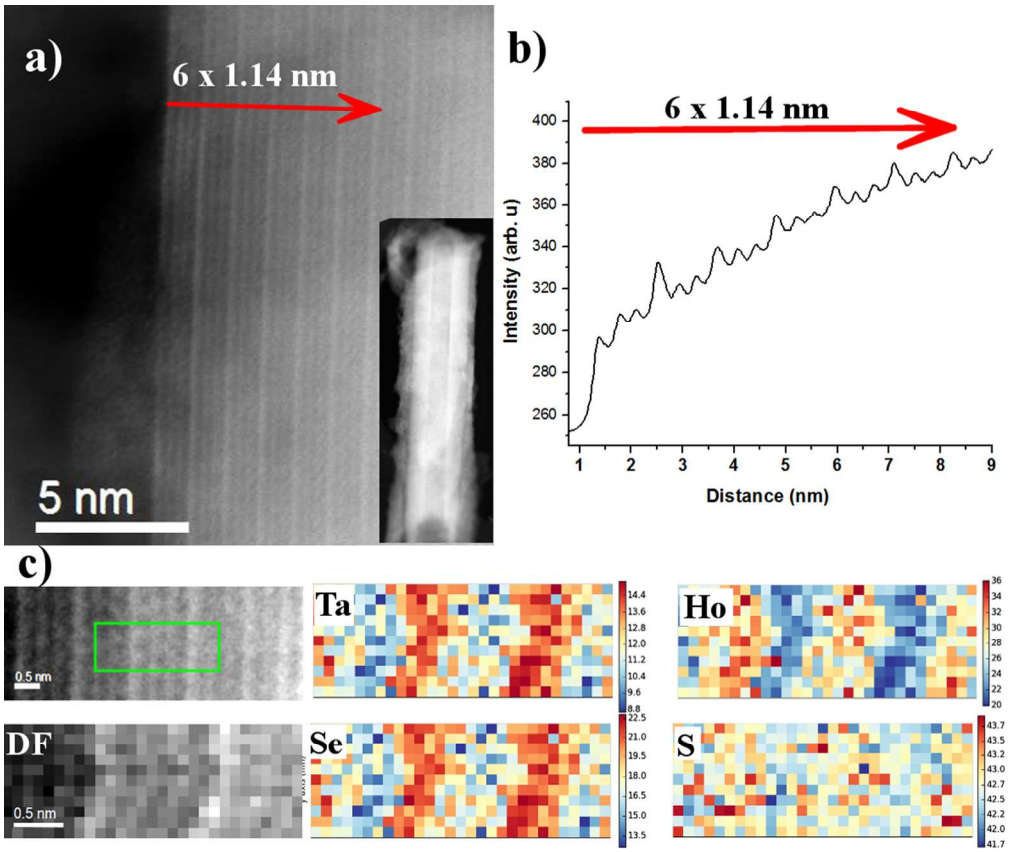

227x191mm (132 x 132 DPI)